PAPER • **OPEN ACCESS**

Integrated thermo-optic phase shifters for laser-written photonic circuits operating at cryogenic temperatures

Journal of Physics: Photonics

PAPER

Integrated thermo-optic phase shifters for laser-written photonic circuits operating at cryogenic temperatures

Francesco Ceccarelli[1], Jelena V Rakonjac[2], Samuele Grandi[2], Hugues de Riedmatten[2,3], Roberto Osellame[1] and Giacomo Corrielli[1,*]

[1] Istituto di Fotonica e Nanotecnologie—Consiglio Nazionale delle Ricerche (IFN-CNR), piazza Leonardo da Vinci 32, 20133 Milano, Italy
[2] ICFO—Institut de Ciencies Fotoniques, The Barcelona Institute of Science and Technology, 08860 Castelldefels (Barcelona), Spain
[3] ICREA—Institució Catalana de Recerca i Estudis Avançats, 08015 Barcelona, Spain
[*] Author to whom any correspondence should be addressed.

E-mail: giacomo.corrielli@cnr.it

Keywords: integrated photonic circuit, cryogenic light modulator, thermo-optic phase shifter, reconfigurable photonics, femtosecond laser waveguide writing, glass photonic chip

Supplementary material for this article is available online

OPEN ACCESS

RECEIVED
16 May 2024

REVISED
12 September 2024

ACCEPTED FOR PUBLICATION
30 September 2024

PUBLISHED
25 October 2024

Abstract

Integrated photonics offers compact and stable manipulation of optical signals in miniaturized chips, with the possibility of changing dynamically their functionality by means of integrated phase shifters. Cryogenic operation of these devices is becoming essential for advancing photonic quantum technologies, accommodating components like quantum light sources, single photon detectors and quantum memories operating at liquid helium temperatures. In this work, we report on a programmable glass photonic integrated circuit (PIC) fabricated through femtosecond laser waveguide writing (FLW) and controlled by thermo-optic phase shifters both in a room-temperature and in a cryogenic setting. By taking advantage of a femtosecond laser microstructuring process, we achieved reliable PIC operation with minimal power consumption and confined temperature gradients in both conditions. This advancement marks the first cryogenically-compatible programmable FLW PIC, paving the way for fully integrated quantum architectures realized on a laser-written photonic chip.

1. Introduction

Integrated photonics is an enabling technology that plays a central role in a growing number of applications, from signal routing and optical interconnects in high-speed data centers [1, 2], to optical computing [3] and quantum information processing [4]. Waveguide-based photonic integrated circuits (PICs) allow for the coherent manipulation of optical signals in an interferometrically stable fashion and with a miniaturized footprint, even when a large number of components are cascaded. Furthermore, PICs can incorporate integrated light modulators, e.g. by exploiting the thermo-optic or the electro-optic response of the waveguides, thus enabling dynamical programming of their function by means of external electrical signals. All these features make PICs capable of carrying out complex photonic operations that are otherwise impossible.

In recent years, the need for PICs operating at cryogenic temperatures has emerged, largely driven by the rapid development of photonic quantum technologies. Indeed, several essential quantum building blocks, including single-emitter-based quantum light sources [5], solid state quantum memories [6], spin-photon interfaces [7] and superconducting nanowire single-photon detectors (SNSPDs) [8], work from few K down to the mK regime, and their integration in quantum photonic processors requires PICs operating reliably also at this temperature range. In addition, cryogenic PICs could also simplify qubit addressing in trapped-ions quantum computers [9, 10], or could reduce the heat load associated to microwave field delivery in superconducting quantum processors [11].

The first demonstrations of cryogenically compatible PICs manufactured by silicon-on-insulator (SOI), silicon nitride (SiN) and lithium niobate (LN) planar technologies have been recently reported, integrating electro-optic [12–19], magneto-optic [20] or elasto-optic modulators [21]. Another successful strategy for obtaining programmable PICs working at low temperature consists in the integration of micro-electromechanical systems (MEMS) within SiN PICs for modulating their functioning via a mechanical deformation of specific waveguide segments [22, 23]. These devices offer striking speed performances, enabling light amplitude/phase modulation with a bandwidth ranging from a few MHz for MEMS-based devices up to tens of GHz for electro-optic components, and almost null static power dissipation. However, their fabrication relies on the heterogeneous integration of different materials, e.g. barium titanate [15], cerium-substituted yttrium iron garnet [20] or aluminum nitride [21], and typically requires highly sophisticated manufacturing processes. In addition, these kinds of integrated modulators suffer from increased optical losses, and their integration with coherent emitters and quantum memory materials is not straightforward. Due to these reasons, the scalability of these approaches and their applicability to photonic quantum technologies is still under study.

In the case of room-temperature quantum photonic experiments, a common solution for manufacturing reconfigurable PICs consists of using thermo-optic phase shifters (TOPSs), which exploit integrated resistive heaters for locally altering the waveguide effective index via Joule effect. Despite being slower, with bandwidths that reach a few hundreds of kHz in best cases [24, 25], TOPSs can be easily integrated at a large scale of up to thousands within a single device [26], with no significant increase of the chip optical losses. Thanks to these features, TOPS-based PICs are currently the only practical solution for building reconfigurable interferometers operating on a large number of modes [26–28], which are among the building block of state-of-the-art photonic quantum technologies, like photonic quantum computing units [29, 30] or photonic quantum state engineering devices [31, 32]. However, realizing quantum PICs based on TOPSs and operating reliably at cryogenic temperatures is challenging for two main reasons. First, the thermo-optic coefficient of relevant materials for PIC manufacturing drops by several orders of magnitude at cryogenic temperatures [14, 33, 34]. Second, heat dissipation and thermal load management inside a cryostat are non-trivial tasks, especially when trying to avoid temperature gradients at the PIC regions where the temperature-sensitive devices, e.g. SNSPDs or quantum memories, are located. Due to these factors, cryogenically compatible TOPS demonstrations have been very few thus far. [34, 35].

In this work we fabricated a programmable glass PIC by the femtosecond laser waveguide writing (FLW) technique, actuated by means of different TOPSs with variable geometry, and, for the first time, we characterized it both at room temperature and in a cryogenic environment. We show that, in agreement with previous studies from our group [36], a suitable substrate microstructuring quenches thermal diffusion outside the TOPS region and produces a reliable PIC operation with low power dissipation (<3 mW for full 2π phase modulation) in both temperature regimes. FLW glass circuits are a valuable tool in the development of photonic quantum technologies [37], as they show low losses, excellent connectivity with optical fibers, and can include a large number of TOPSs to produce arbitrary unitary linear photonic operations [28, 38]. In addition, FLW PICs are compatible with quantum-dot single photon sources [39], and can integrate both quantum memories [40, 41], diamond SiV centers [42] and SNSPDs [35]. Our result represents the first example of a programmable FLW PIC operating at cryogenic temperatures, thus paving the way to the realization of a complete quantum architecture, fully integrated on a FLW chip.

2. Methods

2.1. Device fabrication

The PIC under study contains three independent Mach–Zehnder interferometers (MZIs), each one encompassing a TOPS on one arm for controlling the internal phase, and thus behaving as an integrated light intensity modulator. For each MZI we varied the TOPS length, in order to study the dependence of its efficiency from this geometrical parameter. The PIC was entirely fabricated by FLW in glass following a three-step process, consisting in: (i) direct laser writing of the optical waveguides composing the integrated MZIs; (ii) 3D laser ablation of the glass substrate around the waveguides for improving heat confinement during phase shifting operation; (iii) deposition of a metal layer on top of the glass substrate and definition of the resistors by laser ablation of the metal layer. In the following we discuss this process in detail.

Step 1. High quality optical waveguides have been fabricated by focusing a femtosecond-pulsed laser beam, produced by a homemade Yb:KYW cavity-dumped laser oscillator (wavelength of 1030 nm, pulse duration of 300 fs, repetition rate of 1 MHz) inside a 1 mm thick substrate of a commercial boro-aluminosilicate glass (Eagle XG, from Corning). The focusing optic was a 50x microscope objective with numerical aperture of 0.65. Each waveguide was fabricated by overlapping 12 laser scans (pulse energy of 230 nJ) performed at the speed of 40 mm s^{-1}. After laser irradiation, the sample was annealed at a maximum temperature of 750 °C

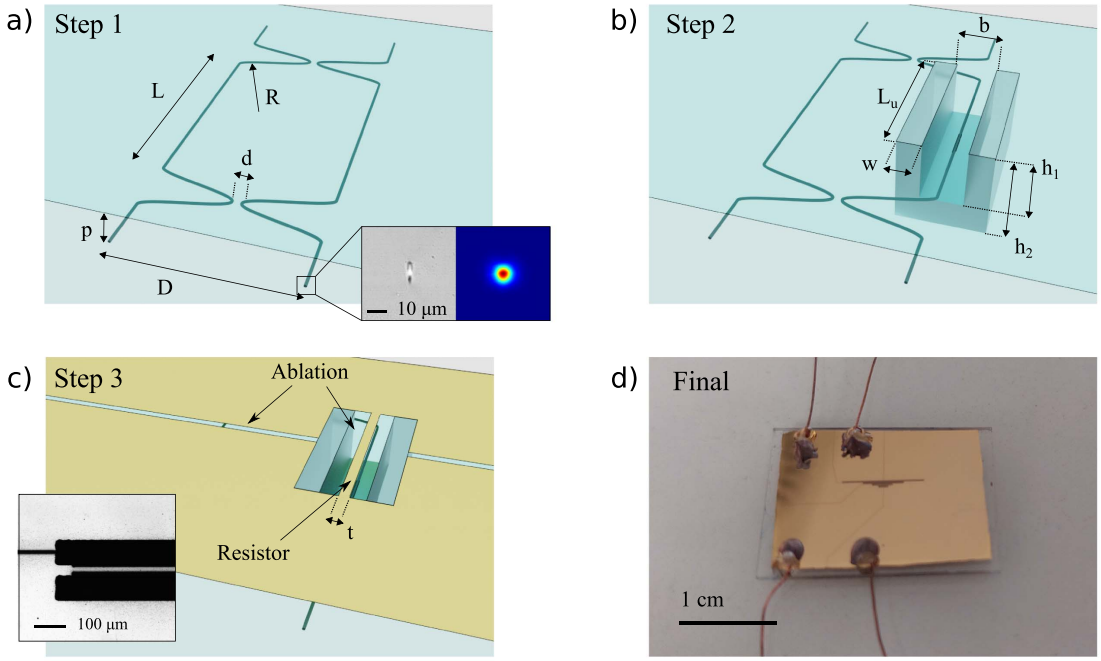

Figure 1. (a) Schematic of the fabricated MZIs. The DCs have been fabricated by concatenating different arches of circumference of radius $R = 35$ mm, which bring the two waveguides of the DC at a minimum interaction distance $d = 4.65\,\mu$m. Waveguide separation D before and after the DCs is 100 μm. Waveguides distance p from the top surface is 50 μm. Three different MZIs have been fabricated with different lengths L of the interferometric arms (1 mm, 5 mm and 10 mm). The inset shows a microscope picture of the waveguide cross section, together with a near-field intensity image of the guided mode, identical for TE and TM polarizations. (b) Schematic of the geometry of the 3D undercuts. For all MZIs: $b = 30\,\mu$m, $W = 70\,\mu$m, $h_1 = 75\,\mu$m and $h_2 = 120\,\mu$m. The length of the MZI arms differ for the values of L_u, which are 1 mm, 4 mm and 8 mm. (c) Schematic of the metal film patterning. Laser ablation is used to narrow the lateral width of the resistive heaters to the value of $t = 15\,\mu$m and to isolate large pads for electrical connections. In the inset we show a white-light microscope image of one of the bridge coated with gold, after the ablation of the resistor edges and the definition of the electrical pads. (d) Photograph of the device at the end of the fabrication process.

for a total annealing duration of 24 h (full annealing process described in [43]). The waveguides fabricated in this way show single mode behavior at 606 nm wavelength ($1/e^2$ mode diameter of ≈2.5 μm, see inset of figure 1(a)), propagation losses <0.2 dB cm^{-1} and negligible bending losses for bending radii >30 mm, with no appreciable differences for TE and TM polarized light. Using this fabrication recipe, we inscribed in the sample a set of three MZIs, each one obtained by cascading two 50/50 directional couplers (DCs), according to the geometry presented in figure 1(a), which features a radius of curvature $R = 35$ mm. Each MZI was inscribed at a depth $p = 50\,\mu$m, and differ from each other by the length L of the straight waveguide segments between the DCs which form the MZI arms. The values of L implemented are 1 mm, 5 mm and 10 mm. The lateral facets of the sample were polished to optical quality in order to expose the waveguide terminations and enable light coupling.

Step 2. After the fabrication of the photonic circuit, we proceeded with the glass microstructuring around the waveguides, with the goal of creating a 3D heat confining structure for enhancing the efficiency of the thermal phase shifters. To do so, we employed the water-assisted laser ablation technique, which consists of irradiating the sample with focused laser pulses for obtaining direct material removal. This process is performed with the sample immersed in deionized water, which helps to remove the glass debris produced during the machining. With this technique we fabricated deep undercuts around one arm of each MZI, according to the geometry shown in figure 1(b), which leaves the waveguides confined in a suspended glass bridge with a rectangular cross section. For the ablation process we used a train of laser pulses (1030 nm wavelength, 1 ps duration, 20 kHz repetition rate, 1.1 μJ pulse^{-1}) from a commercial source (Pharos, from Light Conversion), focused with a water-immersion microscope objective with 0.5 numerical aperture. We fabricated the undercuts with three different longitudinal lengths L_u of 1 mm, 4 mm and 8 mm. For the structures longer than 1 mm, we also added small reinforcement pillars (one every 1 mm, 30 μm × 50 μm rectangular cross section) that connect the suspended glass bridge to the bottom of the undercut.

Step 3. The TOPSs were fabricated according to the process reported in [36]. A Cr/Au (5/100 nm) film was deposited on the glass substrate with a thermal evaporation process (Moorfield MINILAB-080) and then an annealing step (400 °C for 1 h) was employed to prevent long term drifts of the resistance value (and thus of the induced phase) during the operation at high temperature. The sheet resistance of the Cr/Au metal film at

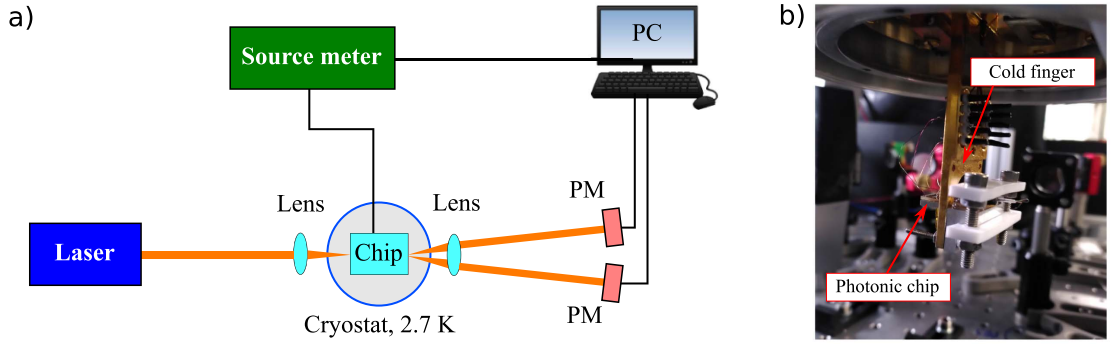

Figure 2. (a) Sketch of the experimental setup used for the PIC characterization. The lenses used for in- and out-coupling of the light in the chip have a focal length of 10 cm. (b) Photograph of the PIC mounted on the cold finger, before the closure of the cryostat.

the end of this process is $R_s \approx 2.0\,\Omega/\square$. After this, we used again FLW for patterning the metal film to define the resistive heaters on top of the suspended waveguides, and to isolate the electrical pads for their connectorization and control (see figure 1(c)). To do so we employed the same laser used in step 2, with different settings: 170 fs pulse duration, 1 MHz repetition rate, 200 nJ pulse energy, 0.25 numerical aperture focusing optics. The heaters fabricated in this way have the same length L_u of the corresponding undercut, and a lateral width t of 15 μm. Finally, we glued four copper wires (three heaters contacts and a common ground) to the metal film at the electrical pads using both an electrically conductive epoxy and a UV curing transparent glue. A photograph of the final device can be seen in figure 1(d).

2.2. Characterization setup

The setup used for the characterization of the PIC is shown in figure 2(a). The PIC was mounted inside a closed-cycle pulse-tube cryostat (Optistat AC-V14, Oxford Instruments; cooling power 0.5 W @ 4 K). The operating pressure inside the sample chamber of the cryostat is $p_C = 9.3 \cdot 10^{-6}$ mbar, and the cold finger reaches a minimum temperature $T_C = 2.7$ K. The PIC itself was glued to an aluminum mount with thermally conductive varnish (GE 7031), and the mount was bolted to the cold finger with Apiezon N grease between the two parts for increased thermal contact. A photograph of the PIC mounted in the cryostat (taken before the closure of the cryogenic chamber) is shown in figure 2(b). Continuous-wave laser light at 606 nm, provided by a commercial laser source (Toptica TA-SHG), is free-space coupled in and out the photonic chip through two lateral viewports mounted on the side walls of the cryogenic chamber, by means of two plano-convex lenses. Two powermeters (PMs) allowed to measure the optical power at the output ports of each MZI simultaneously. Data acquisition with the cryostat turned on was synchronized with the cold finger vibrations, which enabled stable coupling to the waveguides only for $<$300 ms during each cryostat cycle (1.4 Hz). With this setup we measured a chip transmission of $\approx$40% at room temperature and $\approx$20% at cryogenic temperature. We ascribe these limited transmission values to sub-optimal coupling setup. In fact, we were able to measure 75% average MZIs transmission during a preliminary chip inspection performed in a high-precision waveguide positioning setup, and using fiber-butt coupling. The actuation of the TOPSs was performed by means of a programmable sourcemeter (Keysight B2902A), which allows to set electrical currents and voltages with a resolution down to 1 pA and 1 μV, and to measure these quantities with a resolution of 100 fA and 100 nV. Both the sourcemeter and the PMs were connected to a PC, for performing automated measurements.

3. Results and discussion

3.1. Devices characterization

A first characterization of the PIC was performed at room temperature (297.4 K), with the cryostat closed and the sample kept at the operating pressure p_C. We coupled the laser light at one input of each MZI and we measured the output powers $\mathcal{P}_{BAR}$ and $\mathcal{P}_{CROSS}$ at both bar and cross output ports simultaneously, while driving electrical current to the TOPSs. From these measurements we computed the normalized bar transmission $\mathcal{T}_{BAR} = \mathcal{P}_{BAR}/(\mathcal{P}_{BAR} + \mathcal{P}_{CROSS})$ as a function of the dissipated electrical power P for each MZI. These results are shown in figures 3(a)–(c), red dots. For the data fitting (red solid line) we used the

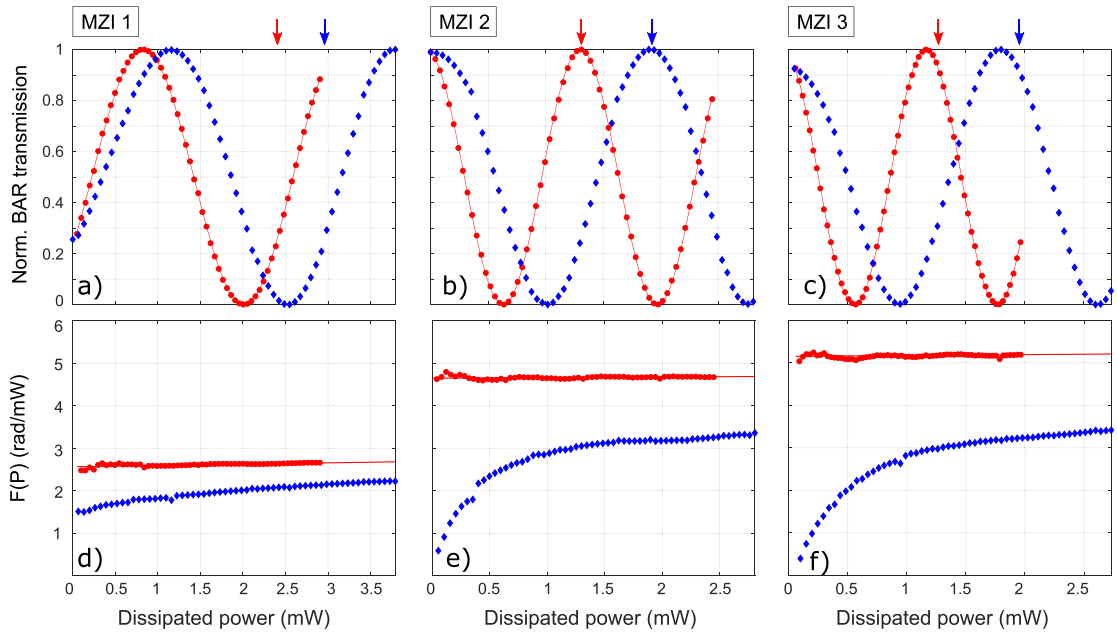

Figure 3. (a)–(c) Experimental characterization of $\mathcal{T}_{\mathcal{BAR}}$ at room (red dots) and cryogenic (blue diamonds) temperature. The three plots (a)–(c) correspond to MZI 1, 2 and 3 (see table 1), respectively. The solid red line is best fit function of room temperature data, according to equations (1) and (2). Red and blue arrows indicate the value of dissipated power needed to attain a 2π phase shift in the two cases. Error bars are smaller than data point markers. (d)–(f) Computed trends of the TOPS efficiencies at room (red dots) and cryogenic (blue diamonds) temperatures as a function of dissipated power, according to equation (4). The solid red line is a plot of $\alpha + \beta P$, according to best fit parameters listed in table 1.

standard transmission model of a balanced MZI with unit visibility:

$$\mathcal{T}_{\mathrm{BAR}}(P) = \frac{1}{2} - \frac{1}{2}\cos\left(\phi_0 + \phi(P)\right). \tag{1}$$

Here, ϕ_0 represents the static optical phase difference between the MZI arms due to fabrication tolerances, while $\phi(P)$ is the optical phase difference induced by heat dissipation as function of P, that, in the case of room temperature operation, is well described by the following relation:

$$\phi(P) = \alpha P + \beta P^2. \tag{2}$$

In this expression, α represents the linear efficiency of the TOPS, while β is a non-linear correction coefficient that accounts for the temperature dependence of the relevant glass thermal parameters, i.e. the thermo-optic coefficient c_{to} and the thermal conductivity k_{glass} (see supplementary material). Even though at room temperature this dependence is very weak and might be ignored in the first place, we decided to include it in our data analysis in order to get a more robust extraction of the static phase ϕ_0, which will be used for the subsequent analysis of the cryogenic behavior. The values of the fitted parameters for all MZIs are listed in table 1. From these measurements we could also retrieve the values of dissipated power $P^A_{2\pi}$ for inducing a 2π phase shift in the case of room temperature operation (also listed in table 1, and indicated in figures 3(a)–(c) with a red arrow), which range from 1.27 mW to 2.40 mW. Such low values are the result of the strong thermal insulation of the glass bridge containing the actuated waveguide. They are significantly lower, by more than an order of magnitude, compared to the usual results achieved under standard pressure conditions and are in good agreement with previous characterizations of similar devices in vacuum environment [36]. It is also worth noting that, differently from the case of operation in standard pressure conditions [36], the length of the TOPS plays an important role in determining the efficiency (and thus the power dissipation) of the device, where longer TOPSs are more efficient than the shorter one. Lastly, we measured the speed of our devices, obtaining a 10%–90% rise time comprised between 200 ms and 400 ms for the three TOPSs, in agreement with our previous studies on similar devices [36].

We then proceeded by characterizing the MZIs with the cryostat turned on, with the cold finger sensor reaching the temperature T_C. An additional thermal probe glued on top of the PIC reported a steady temperature of $T_P = 16.5$ K, thus allowing us to bound the actual temperature of the PIC between T_C and T_P. We attribute this discrepancy to imperfect thermal contact between the PIC and the cold finger and/or between the PIC and the thermal probe. In this condition, we repeated the measurement of $\mathcal{T}_{\mathcal{BAR}}(P)$ for all

Table 1. Summary of the characterization of the different MZIs. L_u indicates the length of the TOPS. $P_{2\pi}$ indicates the value of electrical power required to produce a 2π phase shift at room (A) and cryogenic (B) temperatures. α, β and ϕ_0 are the fit parameters according to the model described by equations (1) and (2), applied to case (A). $\Delta T_M^{2\pi}$ indicates the value of mean temperature increase inside the TOPS for $P = P_{2\pi}^A$, retrieved from numerical simulations (see figure 4(b)). c_{to}^* is the estimated value of the thermo-optic coefficient of Eagle XG at room temperature. Bounds indicate >95% confidence interval for the measured and the fitted data.

Device	L_u (mm)	$P_{2\pi}^A$ (mW)	α (rad mW^{-1})	β (rad mW^{-2})	ϕ_0 (rad)	$P_{2\pi}^B$ (mW)	$\Delta T_M^{2\pi}$ (K)	c_{to}^* (K^{-1})
MZI 1	1	2.40(2)	2.57(2)	0.033(5)	1.0(1)	2.95(2)	69.4(5)	7.28(5)E-6
MZI 2	4	1.35(1)	4.65(2)	0.014(9)	3.35(1)	1.98(2)	19.7(2)	7.32(7)E-6
MZI 3	8	1.27(1)	5.12(3)	0.015(5)	3.39(1)	1.94(2)	10.3(1)	7.17(7)E-6

MZIs, and the results are plotted in figures 3(a)–(c), blue diamonds. Also in this regime we were able to record complete oscillation fringes in the MZI bar transmission, with an observed increase of power dissipation for 2π phase shift of ≈20% for the TOPS with length of 1 mm, and ≈50% for the TOPS with lengths of 4 mm and 8 mm. The actual measured values $P_{2\pi}^B$, indicated with blue arrows in figures 3(a)–(c), are reported in table 1. Importantly, no significant temperature variation at the temperature sensors had been observed during the TOPS actuation in both temperature regimes.

Unlike the room-temperature case, the experimental data acquired at cryogenic temperatures are no longer correctly modeled by equation (2). In particular, the functional shape of $\mathcal{T}_{\mathcal{BAR}}(P)$ is still described by equation (1), but shows a strong and non-linear frequency chirp that reduces the TOPS efficiency for lower values of dissipated power. In order to better quantify this effect and to obtain a direct comparison with the room temperature behavior, we assumed a more generic model for the dependence of $\phi(P)$:

$$\phi(P) = F(P) \cdot P, \tag{3}$$

where $F(P)$ represents the TOPS linear efficiency as a function of the dissipated power. We computed this quantity by inverting numerically the experimental values of $\mathcal{T}_{\mathcal{BAR}}(\mathcal{P})$, according to the formula:

$$F(P) = \frac{\cos^{-1}(1 - 2\mathcal{T}_{\mathcal{BAR}}(P)) - \phi_0}{P}. \tag{4}$$

In doing this operation we used the values of ϕ_0 retrieved from the room temperature data fit (see table 1). The results are shown in figures 3(d)–(f) for all MZIs, computed from both room-temperature (red dots) and cryogenic (blue diamonds) characterization. From these plots one can appreciate that, in the case of room temperature operation, the TOPS efficiency is essentially constant and equal to α. At cryogenic temperatures the efficiency becomes smaller, and drops significantly at low power dissipation values, for which the operating temperature of the TOPSs is closer to T_C. This effect is more pronounced for the longer TOPSs. We attribute this behavior to a significant decrease of the thermo-optic coefficient of Eagle XG glass at low temperature (see supplementary material), an effect similar to the one already reported in the literature for fused silica, silicon and silicon nitride [33, 34].

It is important to mention that the cryostat vibrations prevented us from measuring the modulation speed of our devices at cryogenic temperatures. Therefore, the effect of low temperatures on this property will be subject of future investigations.

3.2. Numerical simulations and discussion

In order to improve our understanding of the TOPS functioning, we performed a finite element numerical simulation of the temperature distribution along the TOPS length during electrical actuation at room temperature. More specifically, the heat equation was solved numerically (using Comsol) under the following assumptions: (i) we neglect longitudinal heat transport in the metal film, and the electrical power dissipation is included in simulations with suitable boundary conditions at the upper surface of the glass bridge (such assumption is justified by considerations reported in the supplementary material); (ii) the thermal conductivity k_{glass} of the Eagle XG is included in the simulation along with its temperature dependence around room conditions [44]; (iii) we model vacuum as a perfect thermally insulating medium, and the only heat dissipation channels from the TOPS are the bridge termination facets and the reinforcement pillars; (iv) The temperature T_0 at the bottom of the glass chip, fixed to 294 K, is not affected by the device operation. This assumption is justified even at cryogenic temperature, since the cooling power of the cryostat is more than 100 times greater than the electrical power used for the TOPS actuation, and, during operation, no significant variation has been measured by the cold finger temperature sensor. The results of these simulations indicate that the average temperature increase ΔT_M inside the suspended glass bridge is almost directly proportional to P, in agreement with the low values of β observed experimentally, and it decreases for longer TOPS (see figure 4(a)) for an equal amount of dissipated power. Then, we

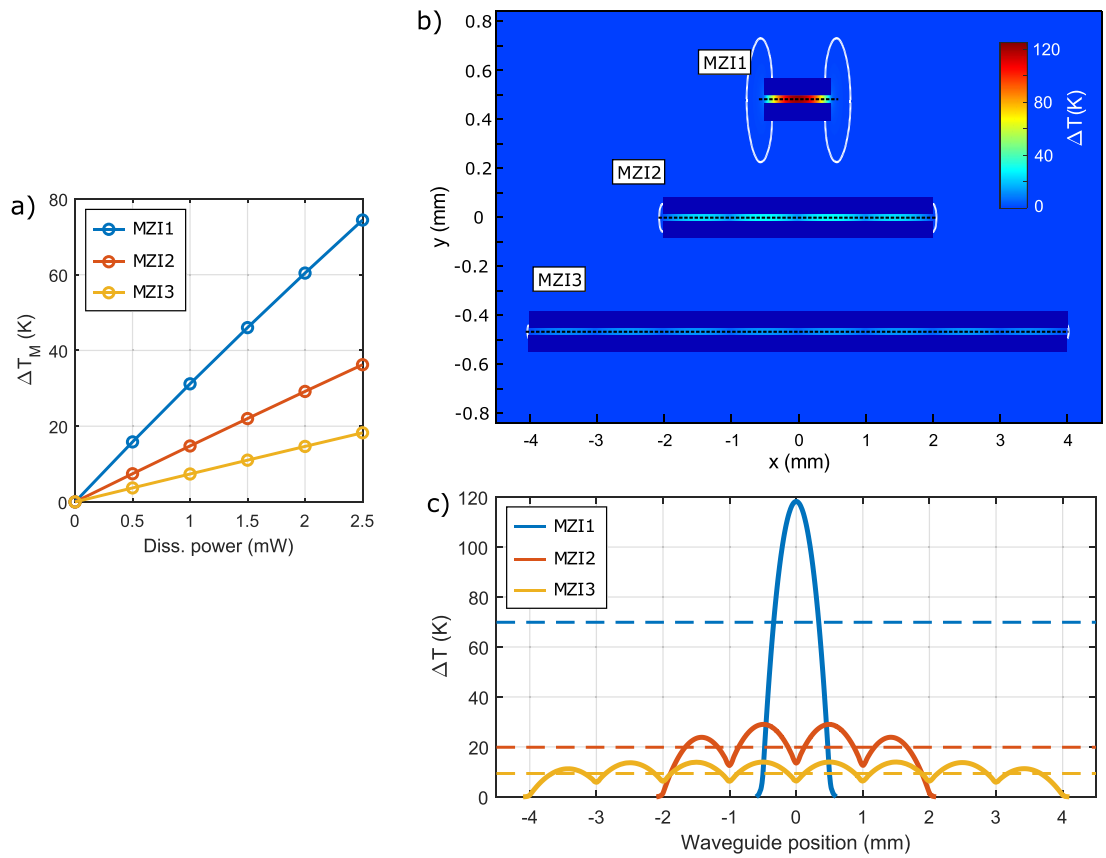

Figure 4. (a) Mean temperature variation ΔT_M along the bridge of the three MZIs as a function of the power dissipation P. Straight segments connect the simulated data points for eye guiding. (b) 2D map of the temperature variation ΔT calculated on the waveguides plane parallel to the sample top surface, with $P = P^A_{2\pi}$ for all MZIs. Dashed black lines indicate the cutlines used for the plots shown in panel (c). White contour lines indicate where temperature increases by 0.5 K. Dark blue rectangles indicate the trenches around the TOPS bridge. (c) Plot of ΔT as a function of the position along the waveguides of the MZIs when $P = P^A_{2\pi}$ (see cutlines in panel (b)). Dashed lines mark the mean temperature variation $\Delta T^{2\pi}_M$. The simulations in all panels consider room temperature and high vacuum starting conditions.

simulated the temperature distribution around the three TOPSs in the case of $P = P^A_{2\pi}$. In figure 4(b) we show the full temperature distribution map calculated on a section plane parallel to the sample top surface, located at the depth of the waveguides. In figure 4(c), instead, we show the results calculated along cutlines corresponding to the heated waveguides of each MZI. For clarity, the position of the cutlines are also indicated as black dashed lines in panel (b) of the same figure. From these results it is possible to appreciate that the temperature gradient has a non-negligible component parallel to the waveguide. This is a direct consequence of the strong insulation provided by the vacuum around the waveguide, which forces the heat to diffuse longitudinally in the bridge. This behavior is substantially different from operation in standard pressure conditions, in which temperature can be considered constant along the whole bridge [36]. In addition, the temperature outside the bridge rapidly drops to T_0. when moving away from the TOPS, especially in the cases of MZI 2 and 3 (white contour line of figure 4(c) indicates $\Delta T = 0.5$ K.) From these simulations we computed the mean temperature variations $\Delta T^{2\pi}_M$ along a waveguide segment of length $L_m = L_u + 0.2$ mm, which includes the temperature decay outside the bridges, and we used these values to estimate the glass thermo-optic coefficient as $c^*_{to} = \lambda/(L_m \Delta T^{2\pi}_M)$ (being λ the light wavelength in vacuum, see the supplementary material for more details). All these results are listed in table 1 and the values of $\Delta T^{2\pi}_M$ are visualized in figure 4(b) as dashed horizontal lines. The accuracy of our simulation is demonstrated by the fact that the values of c^*_{to} obtained for the three MZIs are similar to each other and in good agreement with literature values [36]. Interestingly, the glass pillars underneath the bridge play a major role in determining both the temperature distribution and the MZI power dissipation, as evident by looking at the waviness of the temperature profile for MZI 2 and 3, with the temperature dropping at each pillar. This phenomenon is discussed in more detail in the supplementary material.

These results explain qualitatively also our experimental observations at cryogenic temperature. In particular, a stronger temperature increase for the 1 mm TOPS is in agreement with the fact that the efficiency reported in figure 3(d) does not drop at low power as significantly as in the case of longer TOPSs

reported in figures 3(e) and (f). Indeed, the higher operating temperature of MZI 1 is at the origin of both a higher linearity and an efficiency $F(P)$ that is closer to the one measured at room temperature. This may be a preferable condition if one wants the most similar behavior at the two temperature ranges. Nonetheless, the longer MZIs still show a better overall efficiency, with a lower $P^B_{2\pi}$. The higher efficiency of longer devices, particularly evident at room temperature, is explained by the higher insulation reached by the bridge despite of the presence of reinforcement pillars. More details on the reason why the length affects the efficiency are provided in the supplementary material.

4. Conclusion

In this study we have successfully demonstrated the fabrication and characterization of a programmable glass FLW PIC, equipped with TOPSs that are suitable for operation both at room and cryogenic temperatures. By leveraging the unique 3D microstructuring capabilities of the FLW technology, we achieved reliable PIC operation with minimal power consumption in both temperature regimes. Interestingly, our observations indicate that the drop of the glass thermo-optic coefficient at cryogenic temperatures only marginally impacts the TOPS functioning, given the rapid local heating of the TOPS during actuation. Numerical simulations further corroborate our experimental findings, and show that, in the case of suitable substrate thermalization, relevant temperature gradients extend weakly outside the TOPS region, for distances that range from few μm to hundreds of μm depending on the TOPS geometry, thus not affecting the operation of other integrated components positioned outside this small thermal cross-talk area.

Our findings pave the way to a further optimization of the TOPS geometry, possibly leading to more compact and even more efficient TOPS. In addition, future studies will focus on the investigation of other interesting FLW TOPS properties at cryogenic temperatures, such as their achievable modulation bandwidth and their insertion losses, by employing fiber-pigtailed devices.

In conclusion, our work represents a step forward in the development of quantum photonic technologies, extending the applicability of the FLW platform to the realization of fully integrated quantum photonic devices encompassing building blocks operating at cryogenic temperatures like single photon sources, quantum memories and SNSPDs.

Data availability statement

The data cannot be made publicly available upon publication because they are not available in a format that is sufficiently accessible or reusable by other researchers. The data that support the findings of this study are available upon reasonable request from the authors.

Acknowledgment

RO and GC acknowledge financial support from European Union NextGenerationEU (PNRR MUR Project PE0000023—NQSTI Spoke 7. This work was partially performed at PoliFAB, the micro- and nanofabrication facility of Politecnico di Milano (www.polifab.polimi.it). The authors would like to thank the PoliFAB staff for the valuable technical support. The authors would also like to thank Mario Buffone for the valuable help in the device fabrication.

ORCID iDs

Francesco Ceccarelli https://orcid.org/0000-0001-9574-2899
Jelena V Rakonjac https://orcid.org/0000-0002-0364-9767
Samuele Grandi https://orcid.org/0000-0002-6986-8292
Hugues de Riedmatten https://orcid.org/0000-0002-4418-0723
Roberto Osellame https://orcid.org/0000-0002-4457-9902
Giacomo Corrielli https://orcid.org/0000-0002-1329-8972

References

[1] Havemann R H and Hutchby J A 2001 *Proc. IEEE* **89** 586
[2] Beausoleil R G 2011 *ACM J. Emerg. Technol. Comput. Syst.* **7** 1
[3] Shastri B J, Tait A N, Ferreira de Lima T, Pernice W H, Bhaskaran H, Wright C D and Prucnal P R 2021 *Nat. Photon.* **15** 102
[4] Wang J, Sciarrino F, Laing A and Thompson M G 2020 *Nat. Photon.* **14** 273
[5] Davanco M, Liu J, Sapienza L, Zhang C-Z, De Miranda Cardoso J V, Verma V, Mirin R, Nam S W, Liu L and Srinivasan K 2017 *Nat. Commun.* **8** 889

[6] Zhou Z-Q, Liu C, Li C-F, Guo G-C, Oblak D, Lei M, Faraon A, Mazzera M and de Riedmatten H 2023 *Laser Photonics Rev.* **17** 2300257
[7] Xiong Y, Bourgois C, Sheremetyeva N, Chen W, Dahliah D, Song H, Zheng J, Griffin S M, Sipahigil A and Hautier G 2023 *Sci. Adv.* **9** eadh8617
[8] Esmaeil Zadeh I, Chang J, Los J W, Gyger S, Elshaari A W, Steinhauer S, Dorenbos S N and Zwiller V 2021 *Appl. Phys. Lett.* **118** 190502
[9] Mehta K K, Bruzewicz C D, McConnell R, Ram R J, Sage J M and Chiaverini J 2016 *Nat. Nanotechnol.* **11** 1066
[10] Timpu F, Matt R, Piacentini S, Corbelli G, Marinelli M, Hempel C, Osellame R and Home J 2022 *European Conf. and Exhibition on Optical Communication* (Optica Publishing Group) p We5–70
[11] Lecocq F, Quinlan F, Cicak K, Aumentado J, Diddams S and Teufel J 2021 *Nature* **591** 575
[12] Pintus P, Singh A, Xie W, Ranzani L, Gustafsson M V, Tran M A, Xiang C, Peters J, Bowers J E and Soltani M 2022 *Optica* **9** 1176
[13] Eltes F *et al* 2020 *Nat. Mater.* **19** 1164
[14] Chakraborty U, Carolan J, Clark G, Bunandar D, Gilbert G, Notaros J, Watts M R and Englund D R 2020 *Optica* **7** 1385
[15] Lee B S, Kim B, Freitas A P, Mohanty A, Zhu Y, Bhatt G R, Hone J and Lipson M 2020 *Nanophotonics* **10** 99
[16] Youssefi A, Shomroni I, Joshi Y J, Bernier N R, Lukashchuk A, Uhrich P, Qiu L and Kippenberg T J 2021 *Nat. Electron.* **4** 326
[17] Lomonte E, Wolff M A, Beutel F, Ferrari S, Schuck C, Pernice W H and Lenzini F 2021 *Nat. Commun.* **12** 6847
[18] Gehl M, Long C, Trotter D, Starbuck A, Pomerene A, Wright J B, Melgaard S, Siirola J, Lentine A L and DeRose C 2017 *Optica* **4** 374
[19] Thiele F *et al* 2022 *J. Phys. Photon.* **4** 034004
[20] Pintus P *et al* 2022 *Nat. Electron.* **5** 604
[21] Dong M, Clark G, Leenheer A, Zimmermann M, Dominguez D, Menssen A, Heim D, Gilbert G, Englund D and Eichenfield M 2021 *Nat. Photon.* **16** 59
[22] Beutel F, Grottke T, Wolff M A, Schuck C and Pernice W H 2022 *Opt. Express* **30** 30066
[23] Gyger S, Zichi J, Schweickert L, Elshaari A W, Steinhauer S, Covre da Silva S F, Rastelli A, Zwiller V, Jöns K D and Errando-Herranz C 2021 *Nat. Commun.* **12** 1408
[24] Harris N C, Ma Y, Mower J, Baehr-Jones T, Englund D, Hochberg M and Galland C 2014 *Opt. Express* **22** 10487
[25] Tong W, Yang E, Pang Y, Yang H, Qian X, Yang R, Hu B, Dong J and Zhang X 2023 *Laser Photonics Rev.* **17** 2201032
[26] Suzuki K, Konoike R, Hasegawa J, Suda S, Matsuura H, Ikeda K, Namiki S and Kawashima H 2019 *J. Lightwave Technol.* **37** 116
[27] Taballione C *et al* 2023 *Quantum* **7** 1071
[28] Pentangelo C, Di Giano N, Piacentini S, Arpe R, Ceccarelli F, Crespi A and Osellame R 2024 *Nanophotonics* **13** 2259–70
[29] Maring N *et al* 2024 *Nat. Photon.* **18** 603
[30] Bao J *et al* 2023 *Nat. Photon.* **17** 573
[31] Pont M *et al* 2024 *npj Quantum Inf.* **10** 50
[32] Chen S *et al* 2024 *Phys. Rev. Lett.* **132** 130603
[33] Komma J, Schwarz C, Hofmann G, Heinert D and Nawrodt R 2012 *Appl. Phys. Lett.* **101** 041905
[34] Elshaari A W, Zadeh I E, Jöns K D and Zwiller V 2016 *IEEE Photon. J.* **8** 1
[35] Han H *et al* 2023 *Chin. Opt. Lett.* **21** 081301
[36] Ceccarelli F, Atzeni S, Pentangelo C, Pellegatta F, Crespi A and Osellame R 2020 *Laser Photonics Rev.* **14** 2000024
[37] Corrielli G, Crespi A and Osellame R 2021 *Nanophotonics* **10** 3789
[38] Dyakonov I, Pogorelov I, Bobrov I, Kalinkin A, Straupe S, Kulik S, Dyakonov P and Evlashin S 2018 *Phys. Rev. Appl.* **10** 044048
[39] Antón C *et al* 2019 *Optica* **6** 1471
[40] Rakonjac J V, Corrielli G, Lago-Rivera D, Seri A, Mazzera M, Grandi S, Osellame R and de Riedmatten H 2022 *Sci. Adv.* **8** eabn3919
[41] Zhang X *et al* 2023 *Sci. Adv.* **9** eadf4587
[42] Koch M K, Hoese M, Bharadwaj V, Lang J, Hadden J P, Ramponi R, Jelezko F, Eaton S M and Kubanek A 2022 *ACS Photon.* **9** 3366
[43] Nayak A S *et al* 2021 *Appl. Opt.* **60** D129
[44] Corning Eagle XG glass datasheet 2021 available at: www.corning.com/media/worldwide/cdt/documents/EAGLE%20XG_PI%20Sheet_2021.pdf